University of Tehran

Earth Observation and Geomatics Engineering

Online ISSN: 2588-4360

Homepage: https://eoge.ut.ac.ir/

Monitoring Surface Displacement at the Tang Mud Volcano (Southern Iran) Using SBAS-InSAR and Sentinel-1 Time Series Analysis

Fatemeh Imanpour[1,2] , **Mehdi Akhoondzadeh**[3]✉ , and **Arash Fathollahi**[4]

1. School of Surveying and Geospatial Engineering, Collage of Engineering, University of Tehran, Tehran, Iran.
   E-mail: Imanpour.fatemeh@ut.ac.ir
2. Image processing & Remote Sensing, National Cartographic Center (NCC), Tehran, Iran.
3. Corresponding author, School of Surveying and Geospatial Engineering, Collage of Engineering, University of Tehran, Tehran, Iran.
   E-mail: makhonz@ut.ac.ir
4. Department of Remote Sensing, Faculty of Social Sciences, Mohaghegh Ardabili University, Ardabil, Iran.
   E-mail: arashfathollahi.af@gmail.com

Article Info

Article type:
Research Article

Article history:
Received 2025-07-19
Received in revised form 2025-09-20
Accepted 2025-11-22
Available online 2026-06-02

Keywords:
Surface Displacement
Tang Mud Volcano
SBAS-InSAR
Sentinel-1 SAR
Time Series Analysis.

ABSTRACT

Mud volcanoes are dynamic surface expressions of deep over pressured fluids and gases, requiring precise monitoring to understand their behavior and related hazards. This study investigates ground deformation at the Tang Mud Volcano in southeastern Iran using the Small Baseline Subset (SBAS) InSAR technique applied to 16 Sentinel-1 IW SLC images acquired from December 31, 2023, to December 13, 2024.

Data were processed using the GMTSAR toolbox under a Linux environment, supported by SNAP and GMT. Both Ascending and Descending tracks were analysed to validate deformation signals across viewing geometries. Interferometric analysis included co-registration, baseline estimation, interferogram generation, Goldstein filtering, phase unwrapping, and time-series inversion using Singular Value Decomposition (SVD). Coherence and standard deviation maps ensured data quality.

Results show minimal displacement at the main vent (P1), with cumulative deformation limited to approximately +5 mm, indicating a stable structure. In contrast, a nearby flank area (P2) experienced significant uplift (~+47 mm), suggesting active subsurface processes such as fluid migration or sediment extrusion. Despite the relatively stable behavior observed at the Tang mud volcano itself, the adjacent areas demonstrated significant uplift of up to 6 cm. This level of deformation, occurring over a one-year observation period, highlights the geodynamic activity in parts of the Kahir region. Velocity maps revealed localized deformation rates in mm/year, correlating with fault structures and internal pressure variations.

Time-series analysis highlighted contrasting deformation trends at P1 and P2. The integrated interpretation confirms the effectiveness of SBAS-InSAR in detecting subtle, spatially variable deformation and enhances understanding of the volcano's internal dynamics. These findings provide valuable insight for geohazard assessment and long-term monitoring of mud volcanoes in tectonically active regions.

Cite this article: Imanpour, F., Akhoondzadeh, M., & Fathollahi, A. (2025). Monitoring Surface Displacement at the Tang Mud Volcano (Southern Iran) Using SBAS-InSAR and Sentinel-1 Time Series Analysis. *Earth Observation and Geomatics Engineering*, Volume 9, Issue 2, Pages 17-27. http//doi.org/ 10.22059/eoge.2025.398932.1182

Publisher: University of Tehran.
DOI: http//doi.org/10.22059/eoge.2025.398932.1182

1. Introduction

Mud volcanoes (MVs) are remarkable geological features resulting from the extrusion of fine-grained, water-saturated sediments mixed with gases such as methane, carbon dioxide, and nitrogen. These structures often resemble volcanic cones or domes. They are commonly associated with tectonically active regions, where compressional forces and rapid sedimentation create over-pressured zones in the Earth's crust. Although they are termed "volcanoes", their mechanism is entirely sedimentary and hydrogeological rather than magmatic (Kopf, 2002). The internal structure of a typical conical mud volcano consists of a central feeder channel, pierced sediments, mud breccia layers, and various vents including gryphons and salses (Figure 1) (Dimitrov, 2002).

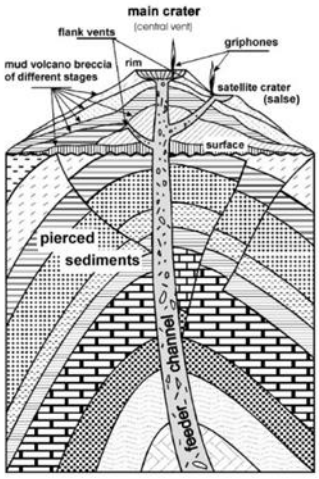

Figure 1. Basic structure and main elements of a conical mud volcano (Dimitrov, 2002).

Globally, mud volcanoes have been identified in more than 44 onshore and 21 offshore regions (Milkov, 2005). They are frequently found in convergent margins, accretionary prisms, and sediment-rich continental slopes. Examples include the Mediterranean Ridge, Black Sea, Gulf of Mexico, Caspian Sea, and the Makran coast (Dimitrov, 2002; Milkov, 2005). Their morphologies vary widely, ranging from steep conical mounds to broad ridges and even caldera-type depressions, often featuring vents, salses, and gryphons (Dimitrov, 2002; Snead, 1964). The materials expelled—commonly referred to as mud breccia—include clay-rich fluids with rock fragments sourced from depths up to 15 kilometers (Milkov, 2005). In Iran, especially along the Makran subduction zone and in regions like Tange-Beres, active mud volcanoes are well-documented. These features are strongly influenced by the ongoing convergence of the Arabian and Eurasian plates and are thought to be surface expressions of deeper geodynamic activity. Field studies in the Makran region have described numerous active cones and ridges formed by the upwelling of mud along fault zones and fractures (Snead, 1964).

In the field of geomatics, various methods have been developed for monitoring surface deformation, among which the Global Positioning System (GPS) and Interferometric Synthetic Aperture Radar (InSAR) are widely applied for tracking crustal displacement. In this study, the Small Baseline Subset InSAR (SBAS-InSAR) technique is employed to monitor and quantify ground deformation in the Tang area, located in Sistan and Baluchistan Province. By comparing phase differences in radar images acquired at different times, the InSAR technique enables high-precision detection of surface displacements (Crosetto et al., 2016). However, in arid and semi-arid regions—where sparse vegetation and surface heterogeneity lead to fewer high-SNR pixels—PS-InSAR performance is constrained, as fewer permanent scatterers are available for accurate deformation modeling (Crosetto et al., 2016; Even et al., 2021).

To overcome these limitations, the Small Baseline Subset (SBAS) InSAR technique was adopted. SBAS combines interferometric pairs with short spatial and temporal baselines, making it more robust in low-coherence environments and allowing it to effectively mitigate temporal decorrelation, phase noise, atmospheric disturbances, and DEM-related errors (Ruiz-Armenteros et al., 2016). Unlike PSI, which primarily relies on stable reflectors and is therefore better suited for urban and semi-industrial environments (Ferretti et al., 2001), SBAS exploits the statistical behavior of distributed scatterers rather than sparse point targets. This enables SBAS to generate reliable displacement time series in natural terrains such as mud volcanoes, where clay-rich soils, moisture variability, and vegetation changes often reduce coherence and limit the number of permanent scatterers (Crosetto et al., 2016; Even et al., 2021; Syahputri et al., 2021).

Numerous studies have demonstrated the effectiveness of SBAS in analyzing volcanic and sedimentary deformation dynamics. For example, Lanari et al. (2004) and Casu et al. (2006) successfully applied SBAS time-series to model volcanic activity in Vulcano Island, retrieving both cumulative and oscillatory displacement patterns. Within Iran, Babaee et al. (2020) in the Qazvin plain and Mirzadeh et al. (2021) in the Yazd–Ardakan basin confirmed that SBAS performs better than PSI in fine-grained, compressible soils, providing stable displacement reconstructions despite temporal decorrelation. These findings highlight that SBAS can effectively monitor wide areas at monthly or even weekly intervals, delivering robust time-series with low RMS error, even in the presence of atmospheric noise or surface variability.
In this study, we apply SBAS-InSAR to the Tang mud volcano in southeastern Iran. Both Ascending and Descending Sentinel-1 datasets were processed, and ERA5-based atmospheric corrections were applied to enhance accuracy. This dual-geometry approach ensures cross-validation, improves robustness, and provides novel insights into subtle, spatially heterogeneous deformation in a semi-arid, geohazard-prone environment.

The main research question addressed in this study is: Can SBAS-InSAR time-series analysis of Sentinel-1 imagery, using both Descending and Ascending datasets, reliably detect and characterize subtle but spatially heterogeneous deformation at the Tang mud volcano in southeastern Iran?

The remainder of this paper is structured as follows: Section 2 describes the case study; Section 3 presents the methodological framework; Section 4 discusses the results; and Section 5 provides conclusions and implications.

2. Case Study

The study was carried out in the Tang area, located in the Konarak–Kahir region of Sistan and Baluchistan Province, southeastern Iran (Figure 2).

In Figure 2, the top-right map shows the position of Sistan and Baluchistan Province within the country. The top-left panel presents the elevation map of the Konarak–Kahir region, where the study area is located. Elevation ranges from −62.9 to 1070.2 meters. The bottom panel provides a detailed satellite view from Google Earth, showing the Tang mud volcano site near the Kahir district. The red outline indicates the regional boundary considered for analysis, and the yellow marker pinpoints the Tang cone.

This region features a semi-arid climate, minimal vegetation cover, and surface heterogeneity, making it a suitable site for remote sensing analysis. The elevation within the study area varies from coastal lowlands to inland heights exceeding 1000 meters. The Tang cone, marked in the satellite image, represents one of the most prominent mud volcanoes in the area and was selected for ground deformation monitoring and morphological analysis.

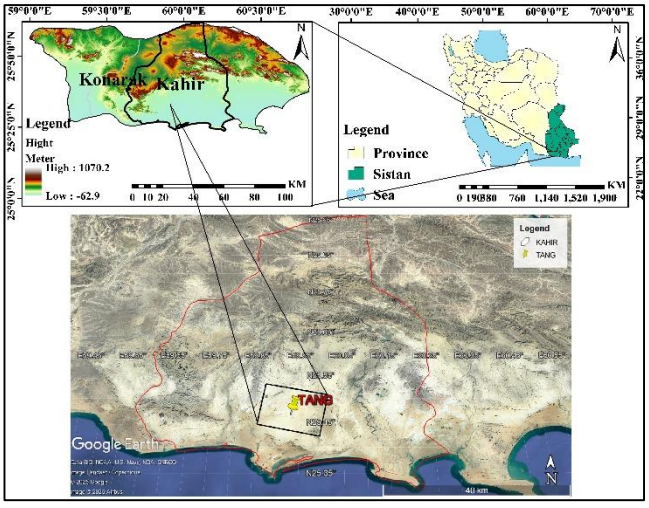

Figure 2. Location of the study area in southeastern Iran.

3. Methodology

The methodological framework employed in this study is based on the Small Baseline Subset (SBAS) InSAR time-series technique, which is widely recognized as an effective approach for retrieving ground displacement signals in challenging environments such as mud volcanoes. Figure X illustrates the end-to-end workflow, consisting of three main stages: (i) data and pre-processing, (ii) InSAR and interferometric processing, and (iii) post-processing, time-series inversion, corrections, and product generation. This workflow chart ensures a concise overview of the methodological framework adopted in this study. To ensure robustness, both Descending and Ascending Sentinel-1 datasets were processed.

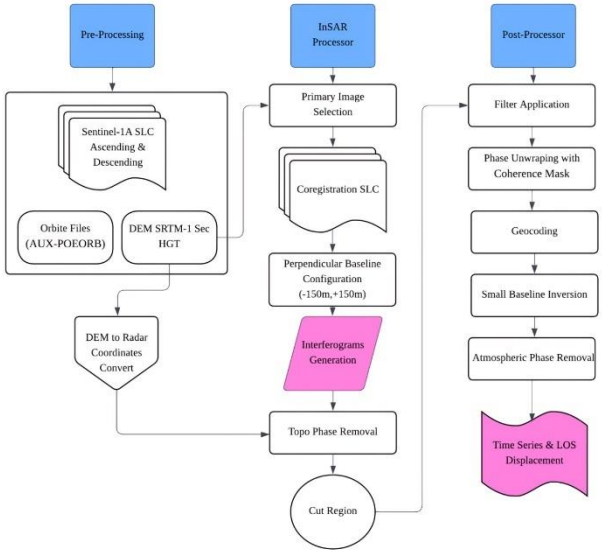

Figure 3. Workflow of the SBAS-InSAR processing steps.

3.1 Data and Pre-processing

In this study, Sentinel-1 synthetic aperture radar (SAR) data provided by the European Space Agency (ESA) were used to derive the displacement time series of the Tang mud volcano. A total of 31 Single Look Complex (SLC) images from both Ascending and Descending orbits were acquired, spanning the period from 28 December 2023 to 13 December 2024. The dataset consists of Sentinel-1A acquisitions in C-band with a central frequency of ~5.405 GHz (wavelength ~5.6 cm) in Interferometric Wide Swath (IW) mode using the TOPS acquisition strategy, providing spatial resolution of ~5 m × 20 m in range and azimuth. All images were acquired in VV polarization, which was selected due to its superior temporal coherence in semi-arid environments.

The spatial and temporal distribution of the Sentinel-1 acquisitions is illustrated in the baseline–time graphs for both Descending and Ascending datasets (Figures 4 and 5). These plots demonstrate the selection of interferometric pairs with short perpendicular baselines to preserve

coherence. The complete specifications of the SAR images, including acquisition dates, orbit paths, and viewing geometries, are provided in Tables 1 and 2.

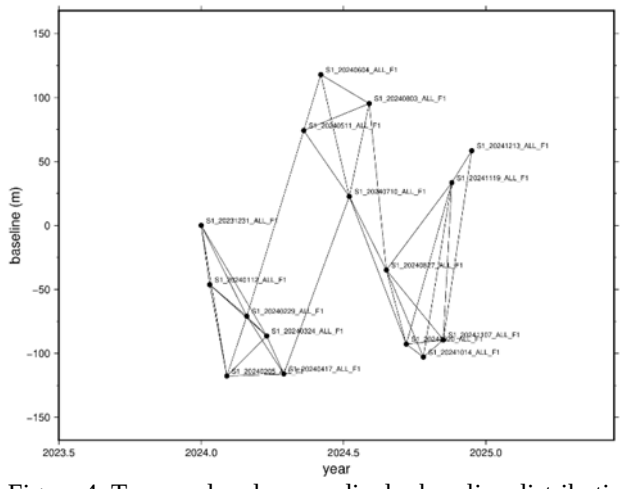

Figure 4. Temporal and perpendicular baseline distribution of the 16 Sentinel-1 Descending images used in this study.

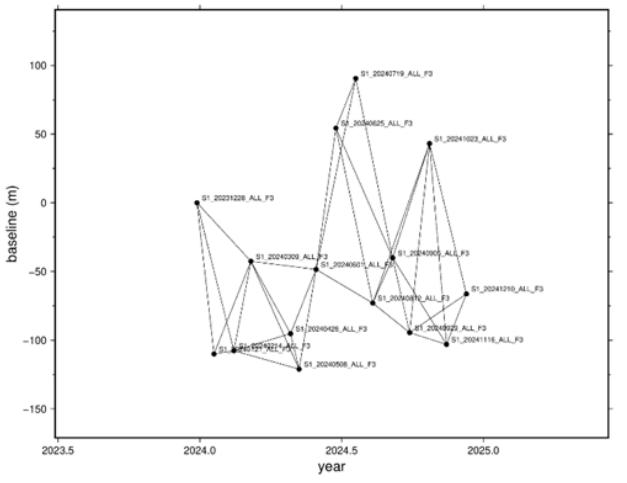

Figure 5. Temporal and perpendicular baseline distribution of the 15 Sentinel-1 Ascending images used in this study.

Table 1. Specifications of the Sentinel-1 SAR Descending images used in this study

No.	Date	Orbit	Path	Pass
1	2023-12-31	51892	20	Descending
2	2024-01-12	52067	20	Descending
3	2024-02-05	52417	20	Descending
4	2024-02-29	52767	20	Descending
5	2024-03-24	53117	20	Descending
6	2024-04-17	53467	20	Descending
7	2024-05-11	53817	20	Descending
8	2024-06-04	54167	20	Descending
9	2024-07-10	54692	20	Descending
10	2024-08-03	55042	20	Descending
11	2024-08-27	55392	20	Descending
12	2024-09-20	55742	20	Descending
13	2024-10-14	56092	20	Descending
4	2024-11-07	56442	20	Descending
15	2024-11-19	56617	20	Descending
16	2024-12-13	56967	20	Descending

Table 2. Specifications of the Sentinel-1 SAR Ascending images used in this study

No.	Date	Orbit	Path	Pass
1	2023-12-28	51856	159	Ascending
2	2024-01-21	52206	159	Ascending
3	2024-02-14	52556	159	Ascending
4	2024-03-09	52906	159	Ascending
5	2024-04-26	53606	159	Ascending
6	2024-05-08	53781	159	Ascending
7	2024-06-01	54131	159	Ascending
8	2024-06-25	54481	159	Ascending
9	2024-07-19	54831	159	Ascending
10	2024-08-12	55181	159	Ascending
11	2024-09-05	55531	159	Ascending
12	2024-09-29	55881	159	Ascending
13	2024-10-23	56231	159	Ascending
14	2024-11-16	56581	159	Ascending
15	2024-12-10	56931	159	Ascending

Given that the study area is located close to the sea, the satellite image frames show that in the Descending geometry (Figure 6) the sea occupies a smaller portion of the frame compared with the Ascending geometry (Figure 7). In this study, both Descending and Ascending datasets were processed to ensure reliability and to provide complementary viewing geometries. In the Descending mode, the image swaths (IW1, IW2, and IW3) are arranged from right to left, whereas in the Ascending mode they are ordered from left to right. Since the study area is located on the right side of the Descending frames, the IW1 swath covers the target region, while in the Ascending frames the corresponding coverage is provided by the IW3 swath.

Figure 6. Satellite image of the area (yellow area) in Descending mode (Patch = 20 Frame = 505).

Figure 7. Satellite image of the area (yellow area) in Ascending mode (Patch = 159 and Frame = 80).

A master image centered in the temporal/perpendicular-baseline cloud was chosen to minimize decorrelation. All SLCs were co-registered to the master with TOPS-specific refinements (burst debursting, azimuth co-registration, Enhanced Spectral Diversity) to ensure sub-pixel accuracy and to avoid azimuth mis-registration artifacts.

To preserve coherence in semi-arid terrain, small perpendicular baselines (±150–200 m) and short temporal separations were enforced, balancing network density against decorrelation (Berardino et al., 2002; Hanssen, 2001). The SRTM DEM was mapped into radar geometry to remove the simulated topographic phase.

For an unwrapped interferogram between epochs t_a and t_b at location x, the interferometric phase is calculated as shown in Equation (1):

$$\phi(x) = 4\pi/\lambda[d(x,t_b)-d(x,t_a)] + \phi^{DEM}(x) + \phi^{atm}(x,t) + \phi^{orb}(x,t) + \varepsilon(x,t) \quad (1)$$

where d is LOS displacement (positive toward the sensor); ϕ^{DEM} residual topography from DEM error; ϕ^{atm} atmospheric phase screen (APS); ϕ^{orb} long-wavelength orbital ramps; and ε decorrelation/thermal noise (Hanssen, 2001).

3.2 InSAR and Interferometric Processing

Co-registered SLCs were paired according to the small-baseline criterion, building a redundant but sparse interferogram network that limits decorrelation while retaining temporal sampling (Berardino et al., 2002; Lanari et al., 2007). Interferograms were generated and the simulated DEM phase was subtracted.

Interferograms were filtered using the Goldstein–Werner filter to improve phase signal-to-noise ratio. Phase unwrapping was carried out with the Minimum-Cost Flow algorithm (SNAPHU; Goldstein & Werner, 1998; Chen & Zebker, 2002), constrained by coherence masks to minimize errors in low-coherence zones. The unwrapped interferograms were then geocoded to WGS84/UTM Zone 40N for further analysis.

Time series were referenced to a stable, high-coherence area outside the mud-volcano edifice to remove common-mode offsets and to establish a physical zero reference.

3.3 Post-processing and SBAS Time-series Analysis

The unwrapped interferometric phases were inverted using the SBAS approach. A linear system of equations was constructed for all interferograms, and solved via Singular Value Decomposition (SVD) to obtain incremental displacements, cumulative time-series, and average velocity maps.

Atmospheric phase screens, which are spatially correlated but temporally uncorrelated, were mitigated using a combination of temporal filtering and ERA5 reanalysis data. The results were finally geocoded to WGS84/UTM Zone 40N for visualization and interpretation.

3.4 Dual-Geometry Analysis

To strengthen robustness, the SBAS workflow was applied separately to both Ascending and Descending datasets. The two results were compared to validate the consistency of deformation patterns. Furthermore, by integrating both viewing geometries, the LOS displacements were decomposed into vertical and east–west horizontal components, enabling a more comprehensive kinematic interpretation of the Tang mud volcano.

3.6 Products and Validation

Primary products include: (i) Mean LOS velocity maps; (ii) cumulative LOS displacement; (iii) LOS time-series at control points;

We report RMS residuals, temporal coherence, and (where available) compare trends with independent observations (e.g., geomorphic indicators or field constraints). Consistency between Ascending and Descending stacks (pattern similarity and magnitude compatibility within expected viewing-geometry differences) provides an internal cross-validation of the deformation signal.

4. Results

In this section, the results of the SBAS-InSAR time series analysis are presented and interpreted comprehensively. The analysis, conducted over the Tang mud volcano using Sentinel-1 imagery from December 2023, to December 2024, includes multiple data layers that offer both spatial and temporal perspectives of surface deformation. The main outputs consist of the coherence map, standard deviation map, cumulative displacement map, time series for points P1 and P2, and the mean velocity map. Each layer contributes uniquely to understanding the dynamics of the deformation process in the region.

The first step in evaluating the reliability of the InSAR analysis involves examining the interferometric coherence images (Figure 8). These maps represent the average interferometric coherence throughout the entire study area for the processed SAR image pairs in both Descending and Ascending geometries.

- In the Descending track (Figure 8, right), areas with high coherence (close to 1) are mainly observed across the central dome and its southern slopes, indicating stable radar backscatter and favorable conditions for SBAS analysis.
- In the Ascending track (Figure 8, left), coherence is

generally consistent with the Descending results, though slight reductions are noticeable in zones affected by vegetation and water bodies, particularly along the coastal margin.

- Areas with low coherence, shown in darker tones, are typically associated with vegetation cover, water surfaces, or zones of frequent surface change.

Overall, the Tang mud volcano exhibits moderate to high coherence in most of its active zones across both geometries, supporting the reliability of subsequent SBAS-derived deformation products.

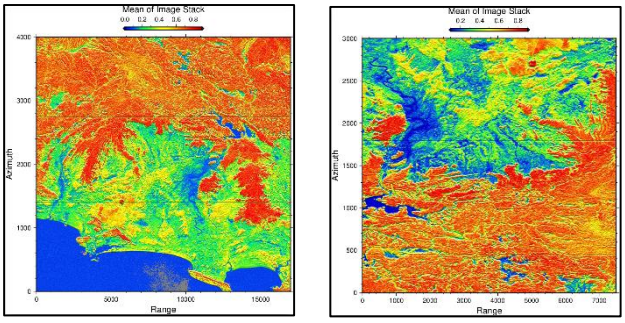

Figure 8. Interferometric coherence maps of the study area derived from Sentinel-1 imagery: (left) Ascending geometry, (right) Descending geometry.

The standard deviation (STD) maps (Figure 9) present the spatial distribution of uncertainty associated with the estimated displacement values for both Ascending and Descending geometries.

- In the Ascending track (Figure 9, left), STD values generally range between 1 mm and 3 mm, with the lowest values concentrated near P1 and P2 (marked in Figure 10). These areas indicate stable radar backscatter and high confidence in the time-series estimates. Peripheral zones, particularly in vegetated patches along the northern margin, show slightly elevated STD values, reflecting reduced phase stability.
- In the Descending track (Figure 9, right), the overall pattern is consistent with the Ascending results. Low STD values dominate the central dome and southern slopes of the Tang mud volcano, whereas higher values are again associated with vegetation and surface heterogeneity in the eastern parts of the study area.

Overall, both geometries confirm that the significant displacement signals, particularly in the dome's center and southern slope, are statistically robust and suitable for quantitative interpretation.

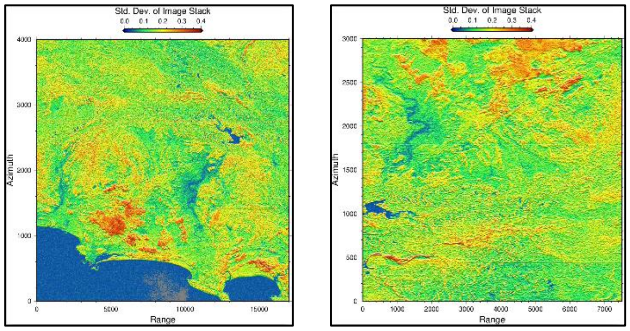

Figure 9. Standard deviation (STD) maps of the Tang mud volcano derived from SBAS-InSAR analysis: (left) Ascending geometry, (right) Descending geometry.

Figure 10 shows the cumulative displacement maps for the Tang mud volcano between the first and last acquisition dates, derived from both Descending (left) and Ascending (right) Sentinel-1 datasets. The color gradients represent the total Line-Of-Sight (LOS) displacement in millimeters, ranging from subsidence (blue) to uplift (yellow–orange).

- In the Descending geometry (Figure 10, left), the southern and southeastern portions of the dome exhibit cumulative uplift exceeding +58 mm, suggesting active mud extrusion and pressurized subsurface flow. Meanwhile, the northern rim and peripheral areas reveal slight to moderate subsidence, likely associated with compaction of previously extruded deposits.
- In the Ascending geometry (Figure 10, right), the overall deformation pattern is consistent with the Descending results, confirming the presence of strong uplift in the south and southeast as well as localized subsidence along the dome's northern margins. Minor variations in magnitude between the two geometries are attributed to differences in viewing geometry and sensitivity to east–west displacement components.

To further analyze these deformation patterns, two coherent points were selected and marked on the displacement maps (Figure 10):

- Point P1 is located at the center of the main dome, representing a relatively stable yet dynamically active zone.
- Point P2 is situated on the southern slope, where the largest uplift gradients are observed.

These cumulative displacement maps highlight the spatial heterogeneity of deformation and support the hypothesis of asymmetric fluid migration within the Tang mud volcano system. They also provide the basis for the subsequent time-series analysis of P1 and P2.

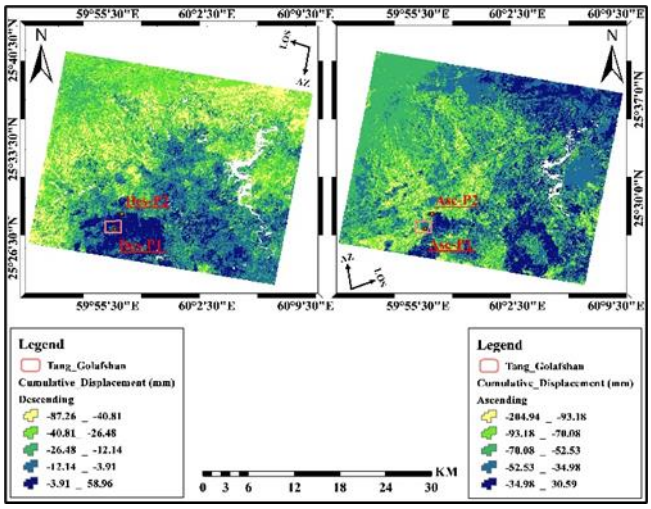

Figure 10. Cumulative LOS displacement maps of the Tang mud volcano between December 2023 and December 2024: (left) Descending geometry, (right) Ascending geometry.

The displacement time-series for Point P1, located at the center of the Tang mud volcano, is illustrated in Figures 11 (Ascending) and 12 (Descending). Both datasets demonstrate that P1 experiences relatively stable deformation over the one-year monitoring period, although the temporal evolution differs slightly between the two geometries.

- In the Ascending track (Figure 11), cumulative displacement shows a modest uplift phase, peaking at approximately +58 mm in late April 2024, followed by a gradual subsidence through mid-2024. By December 2024, the net displacement returns close to equilibrium, stabilizing around +1 to +2 mm.
- In the Descending track (Figure 12), displacement fluctuations are smaller in magnitude, remaining within a narrower range of about ±20 mm. The largest subsidence is observed in July–August 2024 (around −20 mm), with subsequent recovery toward the end of the year, yielding a cumulative displacement close to zero (+5 mm) in December 2024.

Taken together, the results from both geometries indicate that Point P1 does not undergo significant long-term uplift or subsidence. Instead, the observed variations represent episodic but reversible movements, suggesting that the central dome area is in a quasi-equilibrium state. This stability implies that the volcano's core may act as a pressure-relief outlet, gradually releasing mud and gases without generating large-scale deformation. This behavior is consistent with previous studies (e.g., Iio & Furuya, 2018), which reported minimal deformation at the centers of mature and steady-state mud volcanoes, with more pronounced displacement typically occurring at their flanks.

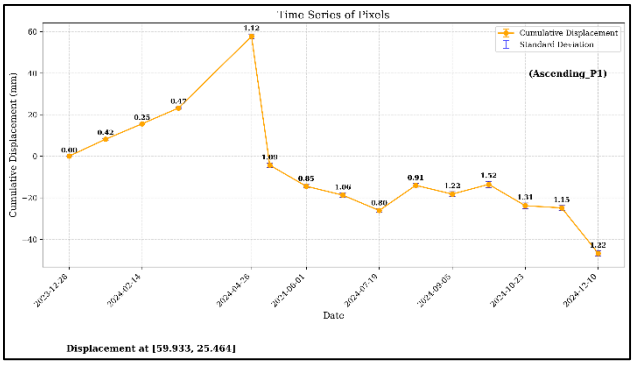

Figure 11. Displacement time-series of Point P1 in Ascending geometry (2023–2024).

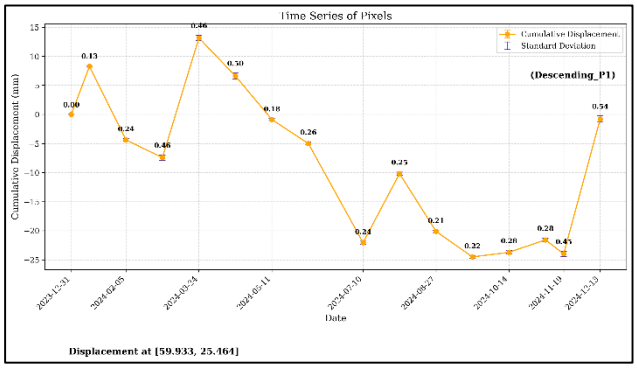

Figure 12. Displacement time-series of Point P1 in Descending geometry (2023–2024).

The displacement time-series for Point P2, located on the southern slope of the Tang mud volcano, is presented in Figures 13 (Ascending) and 14 (Descending). Both geometries consistently reveal a pronounced uplift trend, although the magnitude and temporal evolution show slight differences.

- In the Ascending track (Figure 13), cumulative displacement increases sharply from 0 mm in December 2023 to approximately +59 mm in April 2024. This rapid uplift is followed by a temporary decline to +25 mm in July, likely reflecting slope instability or short-term flow diversion. Deformation resumes thereafter, reaching about +43 mm by December 2024.
- In the Descending track (Figure 14), the displacement pattern follows a similar trajectory but with lower absolute values, peaking at about +31 mm in December 2024. Several inflection points are evident, including rapid uplift episodes in March–May and November, separated by intervals of slowed or reversed deformation in June–August.

STD values at P2 range between ~0.3 and 3 mm, generally lower than at P1, indicating higher coherence and reliability in this slope area. The observed episodic displacement pulses likely reflect intermittent cycles of over-pressurization and fluid discharge, characteristic of active mud volcano dynamics.

The clear upward movement along the southern slope suggests active extrusion and lateral spreading, consistent with inclined conduit structures. This behavior aligns with previous studies (e.g., Iio & Furuya, 2018), which reported that mud volcano flanks typically show larger and less stable deformation compared to their central zones due to lateral fluid and gas migration through fracture systems.

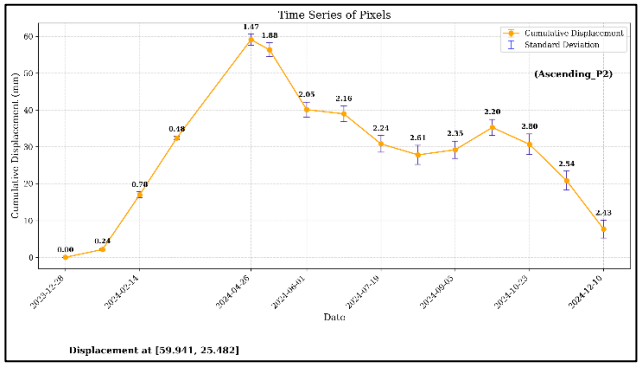

Figure 13. Displacement time-series of Point P2 in Ascending geometry (2023–2024).

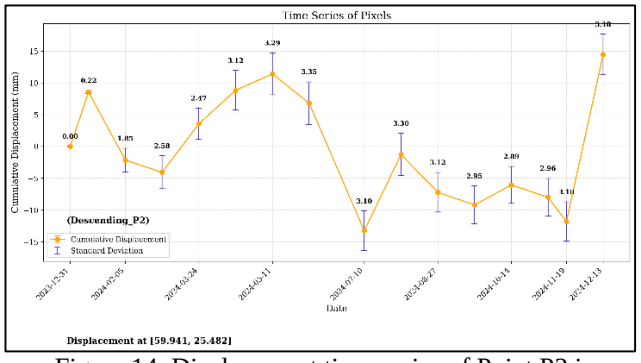

Figure 14. Displacement time-series of Point P2 in Descending geometry (2023–2024).

The mean velocity maps derived from SBAS-InSAR analysis are presented in Figure 15 for both Descending and Ascending geometries. These maps illustrate the average line-of-sight (LOS) deformation rates across the study area during 2023–2024.

- In the Descending geometry, uplift rates locally exceed +44.9 mm/year, particularly concentrated around Point P2 and adjacent southern sectors. Subsidence zones are also detected, with rates as low as −133.3 mm/year, mainly along the northern margins and some southeastern sectors.
- In the Ascending geometry, the overall deformation pattern is consistent with the Descending results, though the magnitudes differ slightly due to varying look angles. Maximum uplift surpasses +42.7 mm/year in the southern dome, while subsidence reaches values below −130.0 mm/year in the northern flank.

The velocity fields from both geometries confirm a radially asymmetric displacement regime, characterized by predominant uplift in the southern and central zones of the dome, and subsidence on the northern and peripheral flanks. This asymmetry is consistent with differential pressure release and fracture-controlled fluid migration within the mud volcano system.

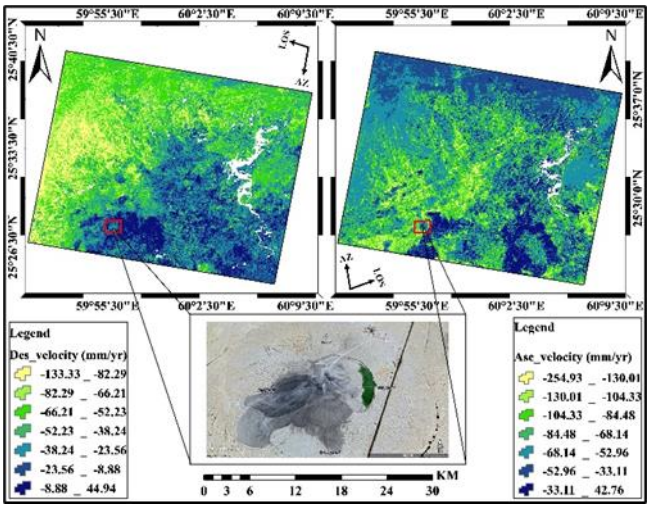

Figure 15. Mean LOS velocity maps from SBAS-InSAR analysis: (left) Descending geometry and (right) Ascending geometry, illustrating uplift in the southern dome (around P2) and subsidence in the northern periphery.

Figure 16 presents the Root Mean Square (RMS) maps of phase residuals from the SBAS-InSAR time series, where the left panel corresponds to the Descending geometry and the right panel to the Ascending geometry. These maps represent the degree of deviation between the observed interferometric phases and the estimated deformation model.

- In the Descending dataset (left), RMS values range between 1.1 mm and 15.7 mm, with the lowest values (1.1–5.4 mm) concentrated in the central and southern sectors, including the Tang mud volcano outlined in the black rectangle. These low RMS values confirm the presence of a coherent and reliable deformation signal over the volcano. Higher RMS values (above 9.9 mm) are mostly distributed across the northern and northeastern margins, reflecting decorrelation effects caused by vegetation cover, surface changes, or moisture variability.
- In the Ascending dataset (right), RMS values range between 2.1 mm and 32.4 mm, showing a similar spatial distribution pattern but with slightly higher deviations. The lowest RMS values (2.1–6 mm) are again concentrated over the Tang mud volcano, confirming the robustness of the phase solutions in this critical area. Larger RMS values (above 18 mm) appear mainly along the northern periphery and foothills, where coherence is typically reduced.

Overall, the consistent presence of low RMS values within the mud volcano boundary across both geometries validates the accuracy and reliability of the deformation time series and velocity estimates, strengthening the interpretations presented in the displacement and velocity analyses.

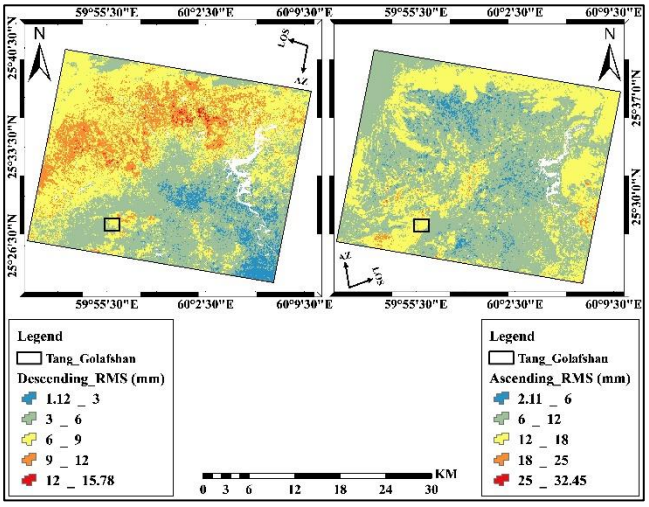

Figure 16. RMS (Root Mean Square) maps of phase residuals from SBAS-InSAR analysis: (left) Descending geometry and (right) Ascending geometry. The black rectangle highlights the Tang Mud Volcano, where low RMS values confirm high signal coherence and robust deformation measurements.

By integrating all geospatial layers and displacement metrics from both Descending and Ascending geometries, a coherent picture of the deformation dynamics in the Tang mud volcano emerges:

- **Stable Zones**: The central and northern parts of the dome (e.g., Point P1) remain nearly static in both datasets, showing minimal displacement, very low deformation rates, and high coherence. These characteristics imply structural stability and limited subsurface activity during the study period.
- **Active Zones**: The southern and southwestern sectors, particularly around Point P2 and the outer lobes, consistently show high velocities and significant cumulative displacements in both geometries. The Ascending track captures slightly larger deformation magnitudes compared to the Descending track, though the spatial patterns are highly consistent. These signals reflect ongoing mud extrusion, with high temporal variability suggesting episodic behavior driven by internal pressure fluctuations, gas release, and possibly climatic or seasonal triggers.
- **Velocity Gradient**: A pronounced radial gradient is observed from the center of the volcano outward, in both Ascending and Descending results, pointing to differential pressure distribution within the mud reservoir or compartmentalized conduit recharge.
- **Error Analysis**: Standard deviation (STD) values remain within acceptable limits (generally <2.5 mm), and the RMS residuals are consistently low over the volcano area (1.1–5.4 mm for Descending and 2.1–6 mm for Ascending). This convergence of low STD and RMS values, especially around P1 and P2, confirms robust phase unwrapping, high temporal coherence, and strong signal integrity across both viewing geometries.

Together, these findings provide a reliable and internally validated picture of the deformation dynamics of the Tang mud volcano, strengthening confidence in the interpretation of uplift at the southern dome and relative stability in the central and northern zones.

5. Conclusion

This study employed the Small Baseline Subset Interferometric Synthetic Aperture Radar (SBAS-InSAR) technique using Sentinel-1 satellite imagery to investigate the spatiotemporal deformation behaviour of the Tang mud volcano in southeastern Iran. Through the integration of coherence analysis, standard deviation assessment, cumulative displacement mapping, velocity estimation, and time-series analysis at selected key points, a comprehensive understanding of surface dynamics and internal activity of the mud volcano was achieved.

Compared with previous studies on mud volcanoes in Azerbaijan, the Caspian region, and East Java, this work introduces the first dual-geometry SBAS-InSAR analysis of the Tang mud volcano. This approach not only validates the deformation signals across two independent viewing geometries but also demonstrates the capability of SBAS-InSAR to operate reliably in semi-arid, low-coherence environments. These contributions make the study both novel and significant for the broader field of geohazard monitoring.

The results reveal significant spatial and temporal deformation patterns. The cumulative displacement map (Figure 10) clearly identifies areas of notable motion, particularly surrounding the Tang mud volcano (P1), and a nearby region (P2) that shows amplified surface movement.

Time-series analysis at P1 (Figure 11 and 12) indicates minor displacement variability within ±20 mm, stabilizing near +5 mm toward the end of the observation period. This limited activity suggests relative surface stability and low eruptive or uplift activity at the volcano during the study period. The near-zero displacement at Point P1 may be attributed to an internal pressure equilibrium beneath the Tang mud volcano. This equilibrium results in structural coherence and reduced deformation in its core.

In contrast, point P2 (Figure 13 and 14) displays a more dynamic displacement trajectory, reaching ~47 mm by December 2024. Such behaviour could be attributed to subsurface fluid migration, lateral mud extrusion, or structural collapse around the flanks of the volcano (Iio & Furuya, 2018). Therefore, the behaviour of Point P2 supports the hypothesis that the Tang mud volcano is undergoing low-frequency but spatially differential activity,

with the central dome remaining stable while peripheral zones like P2 experience more active deformation.

The mean velocity map (Figure 15) complements these findings by delineating long-term displacement rates. The velocity field shows a gradient from stable regions to zones with substantial subsidence or uplift, particularly aligned along structural discontinuities. The sharp gradient in velocity around the volcano boundary further emphasizes the localized nature of the deformation, likely confined to the active conduit system of the volcano.

The RMS map (Figure 16) further substantiates the high quality of the SBAS-InSAR results, particularly over the Tang mud volcano. The consistently low residual errors in this region confirm that the displacement patterns identified—such as the relative stability of the volcano cone and uplift in surrounding areas—are not influenced by noise or decorrelation, but represent genuine ground deformation processes.

Also, the coherence and standard deviation maps (Figures 8 and 9) validate the reliability of derived displacements and support the robustness of our time-series observations.

The comparison of Ascending and Descending results confirms consistent patterns of deformation. The Ascending track corroborates the strong uplift signal near P2 and the relative stability of P1, with only slight differences in displacement magnitude. Integrating both datasets demonstrates that the Tang mud volcano exhibits negligible deformation at its central dome and significant uplift at its southern flank, thereby validating the robustness of the SBAS-InSAR analysis. This cross-geometry agreement reduces uncertainties related to viewing geometry and strengthens confidence that the observed deformation is real rather than an artefact of acquisition geometry.

Cross-analysis of these spatial patterns with geological features underscores that the Tang mud volcano system is controlled by both internal processes (e.g., overpressure, fluid migration, and sediment loading) and external factors such as tectonic setting and lithology. These findings are consistent with previous studies highlighting the episodic nature and structural complexity of mud volcano systems (Mazzini & Etiope, 2017).

Geologically, these findings suggest that the Tang mud volcano is being sustained by a moderately pressurized fluid system. The spatial variation in displacement, with intense localized activity near the flow lobes and quiescent behaviour elsewhere, is indicative of a branching or compartmentalized internal conduit network, a characteristic noted in other active mud volcanoes worldwide (e.g., Mazzini et al., 2017).

The presence of both stable and highly deforming zones within a relatively confined area suggests a complex subsurface architecture, possibly featuring branching conduits and differential pressure regimes. Monitoring such patterns is essential for hazard assessment and understanding fluid–geological interactions in tectonically active regions.

These findings underscore the importance of continuous InSAR monitoring in identifying active deformation zones and understanding the dynamics of mud volcanism with high spatial and temporal resolution.

Overall, the multi-temporal analysis using Sentinel-1 data and the SBAS-InSAR technique has proven effective in capturing both short-term surface fluctuations and long-term deformation trends, offering valuable insights into the behaviour and hazards associated with the Tang mud volcano. The results enhance our understanding of the spatiotemporal behaviour of the Tang system and could inform risk assessments related to subsurface fluid pathways, land use, or potential geological hazards.

By integrating both Descending and Ascending Sentinel-1 datasets, we demonstrated that the Tang mud volcano exhibits negligible deformation at its central dome and significant uplift at its southern flank. The dual-geometry SBAS analysis validates the observed LOS deformation and enhances confidence in the robustness of our findings, underscoring the importance of multi-geometry InSAR for reliable geohazard monitoring in semi-arid volcanic and sedimentary environments.

This study demonstrates that SBAS-InSAR time-series analysis of both Ascending and Descending Sentinel-1 datasets can reliably detect and characterize localized deformation of the Tang mud volcano. The results confirm the robustness of the SBAS approach in semi-arid, low-coherence environments, addressing the main research question and offering valuable insights for geohazard monitoring in the Makran subduction zone. This dual-geometry approach represents the first comprehensive InSAR-based monitoring of the Tang mud volcano and provides a methodological framework for future geohazard studies in similar semi-arid settings.

References

Amini, L., Fathallahzadeh, M., & Kakroodi, A. A. (2023). Monitoring Ground Deformation of Mud Volcanoes Using Radar Interferometric Method (sbas) and Thermal Data Case Study: the South-Eastern Part of the Caspian Sea. *ISPRS Annals of the Photogrammetry, Remote Sensing and Spatial Information Sciences*, *10*, 63-70. https://doi.org/10.5194/isprs-annals-X-4-W1-2022-63-2023

Babaee, S., Mousavi, Z., Masoumi, Z., Malekshah, A. H., Roostaei, M., & Aflaki, M. (2020). Land subsidence from interferometric SAR and groundwater patterns in the Qazvin plain, Iran. *International Journal of Remote Sensing*, *41*(12), 4780-4798. https://doi.org/10.1080/01431161.2020.1724345

Berardino, P., Fornaro, G., Lanari, R., & Sansosti, E. (2003). A new algorithm for surface deformation monitoring based on small baseline differential SAR interferograms. *IEEE Transactions on geoscience and remote sensing*, *40*(11), 2375-2383. https://doi.org/10.1109/TGRS.2002.803792

Bekaert, D. P. S., Hooper, A., & Wright, T. J. (2015). A spatially variable power law tropospheric correction technique for InSAR data. *Journal of Geophysical Research: Solid Earth*, *120*(2), 1345-1356. https://doi.org/10.1002/2014JB011558

Crosetto, M., Monserrat, O., Cuevas-González, M., Devanthéry, N., & Crippa, B. (2016). Persistent scatterer interferometry: A review. *ISPRS Journal of Photogrammetry and Remote Sensing*, *115*, 78-89. https://doi.org/10.1016/j.isprsjprs.2015.10.011

Casu, F., Manzo, M., & Lanari, R. (2006). A quantitative assessment of the SBAS algorithm performance for surface deformation retrieval from DInSAR data. *Remote Sensing of Environment*, *102*(3-4), 195-210. https://doi.org/10.1016/j.rse.2006.01.023

Costantini, M. (2002). A novel phase unwrapping method based on network programming. *IEEE Transactions on geoscience and remote sensing*, *36*(3), 813-821. https://doi.org/10.1109/36.673674

Chen, C. W., & Zebker, H. A. (2001). Two-dimensional phase unwrapping with use of statistical models for cost functions in nonlinear optimization. *Journal of the Optical Society of America A*, *18*(2), 338-351. https://doi.org/10.1364/JOSAA.18.000338

Dimitrov, L. I. (2002). Mud volcanoes—the most important pathway for degassing deeply buried sediments. *Earth-Science Reviews*, *59*(1-4), 49-76. https://doi.org/10.1016/S0012-8252(02)00069-7

Even, M., & Schulz, K. (2018). InSAR deformation analysis with distributed scatterers: A review complemented by new advances. *Remote Sensing*, *10*(5), 744. https://doi.org/10.3390/rs10050744

Ferretti, A., Prati, C., & Rocca, F. (2002). Permanent scatterers in SAR interferometry. *IEEE Transactions on geoscience and remote sensing*, *39*(1), 8-20. https://doi.org/10.1109/36.898661

Goldstein, R. M., & Werner, C. L. (1998). Radar interferogram filtering for geophysical applications. *Geophysical research letters*, *25*(21), 4035-4038. https://doi.org/10.1029/1998GL900033

Hooper, A., Bekaert, D., Spaans, K., & Arıkan, M. (2012). Recent advances in SAR interferometry time series analysis for measuring crustal deformation. *Tectonophysics*, *514*, 1-13. https://doi.org/10.1016/j.tecto.2011.10.013

Hooper, A., Zebker, H., Segall, P., & Kampes, B. (2004). A new method for measuring deformation on volcanoes and other natural terrains using InSAR persistent scatterers. *Geophysical research letters*, *31*(23). https://doi.org/10.1029/2004GL021737

Hanssen, R. F. (2001). Radar interferometry: data interpretation and error analysis. *Dordrecht: Springer Netherlands*. https://doi.org/10.1007/0-306-47633-9_4

Iio, K., & Furuya, M. (2018). Surface deformation and source modeling of Ayaz-Akhtarma mud volcano, Azerbaijan, as detected by ALOS/ALOS-2 InSAR. *Progress in Earth and Planetary Science*, *5*(1), 61. https://doi.org/10.1186/s40645-018-0220-7

Kopf, A. J. (2002). Significance of mud volcanism. *Reviews of geophysics*, *40*(2), 2-1. https://doi.org/10.1029/2000RG000093

Lanari, R., Casu, F., Manzo, M., Zeni, G., Berardino, P., Manunta, M., & Pepe, A. (2007). An overview of the small baseline subset algorithm: A DInSAR technique for surface deformation analysis. *Deformation and Gravity Change: Indicators of Isostasy, Tectonics, Volcanism, and Climate Change*, 637-661. https://doi.org/10.1007/978-3-7643-8417-3_2

Lanari, R., Mora, O., Manunta, M., Mallorquí, J. J., Berardino, P., & Sansosti, E. (2004). A small-baseline approach for investigating deformations on full-resolution differential SAR interferograms. *IEEE transactions on geoscience and remote sensing*, *42*(7), https://doi.org/1377-1386. 10.1109/TGRS.2004.828196

Mazzini, A., & Etiope, G. (2017). Mud volcanism: An updated review. *Earth-Science Reviews*, *168*, 81-112. https://doi.org/10.1016/j.earscirev.2017.03.001

Milkov, A. V. (2005). Global distribution of mud volcanoes and their significance in petroleum exploration as a source of methane in the atmosphere and hydrosphere and as a geohazard. In *Mud Volcanoes, Geodynamics and Seismicity: Proceedings of the NATO Advanced Research Workshop on Mud Volcanism, Geodynamics and Seismicity Baku, Azerbaijan 20–22 May 2003* (pp. 29-34). Dordrecht: Springer Netherlands. https://doi.org/10.1007/1-4020-3204-8_3

Mirzadeh, S. M. J., Jin, S., Parizi, E., Chaussard, E., Bürgmann, R., Delgado Blasco, J. M., ... & Mirzadeh, S. H. (2021). Characterization of irreversible land subsidence in the Yazd-Ardakan plain, Iran from 2003 to 2020 InSAR time series. *Journal of Geophysical Research: Solid Earth*, *126*(11), e2021JB022258. https://doi.org/10.1029/2021JB022258

Ruiz-Armenteros, A. M., Bakon, M., Lazecky, M., Delgado, J. M., Sousa, J. J., Perissin, D., & Caro-Cuenca, M. (2016). Multi-temporal InSAR processing comparison in presence of high topography. *Procedia Computer Science*, *100*, 1181-1190. https://doi.org/10.1016/j.procs.2016.09.278

Syahputri, B. E. A., Anjasmara, I. M., & Widodo, A. (2021). Surface Deformation Detection due to Mud Volcanoes Manifestation in East Java Basin Area using Permanent Scatterer InSAR. In *IOP Conference Series: Earth and Environmental Science* (Vol. 731, No. 1, p. 012008). IOP Publishing. https://doi.org/10.1088/1755-1315/731/1/012008

Sandwell, D., Mellors, R., Tong, X., Wei, M., & Wessel, P. (2011). GMTSAR: An InSAR processing system based on generic mapping tools. https://doi.org/10.2172/1090004

Snead, R. E. (1964). Active mud volcanoes of Baluchistan, west Pakistan. *Geographical Review*, *54*(4), 546-560. https://doi.org/10.2307/21